Technical Note

Estimating Satellite-Derived Bathymetry (SDB) with the Google Earth Engine and Sentinel-2

**Dimosthenis Traganos [1] [iD], Dimitris Poursanidis [2,* iD], Bharat Aggarwal [1],
Nektarios Chrysoulakis [2] [iD] and Peter Reinartz [3] [iD]**

[1] German Aerospace Center (DLR), Remote Sensing Technology Institute, Rutherfordstraße 2,
12489 Berlin, Germany; Dimosthenis.Traganos@dlr.de (D.T.); 851.bharat@gmail.com (B.A.)

[2] Foundation for Research and Technology—Hellas (FORTH), Institute of Applied and Computational
Mathematics, N. Plastira 100, Vassilika Vouton, 70013 Heraklion, Greece; zedd2@iacm.forth.gr

[3] German Aerospace Center (DLR), Earth Observation Center (EOC), 82234 Weßling, Germany;
peter.reinartz@dlr.de

* Correspondence: dpoursanidis@iacm.forth.gr, Tel.: +30-2810-391774

check for
updates

Abstract: Bathymetry mapping forms the basis of understanding physical, economic, and ecological processes in the vastly biodiverse coastal fringes of our planet which are subjected to constant anthropogenic pressure. Here, we pair recent advances in cloud computing using the geospatial platform of the Google Earth Engine (GEE) with optical remote sensing technology using the open Sentinel-2 archive, obtaining low-cost in situ collected data to develop an empirical preprocessing workflow for estimating satellite-derived bathymetry (SDB). The workflow implements widely used and well-established algorithms, including cloud, atmospheric, and sun glint corrections, image composition and radiometric normalisation to address intra- and inter-image interferences before training, and validation of four SDB algorithms in three sites of the Aegean Sea in the Eastern Mediterranean. Best accuracy values for training and validation were $R^2 = 0.79$, RMSE = 1.39 m, and $R^2 = 0.9$, RMSE = 1.67 m, respectively. The increased accuracy highlights the importance of the radiometric normalisation given spatially independent calibration and validation datasets. Spatial error maps reveal over-prediction over low-reflectance and very shallow seabeds, and under-prediction over high-reflectance (<6 m) and optically deep bottoms (>17 m). We provide access to the developed code, allowing users to map bathymetry by customising the time range based on the field data acquisition dates and the optical conditions of their study area.

Keywords: satellite-derived bathymetry; image composition; pseudo-invariant features; sun glint correction; empirical; spatial error; Google Earth Engine; low cost in situ; Sentinel-2; Mediterranean

1. Introduction

Bathymetry is important for understanding how global Earth processes interact as they influence the flow of the sea water carrying heat, salt, nutrients, and pollutants. Bathymetry also aids in understanding the propagation of energy from undersea seismic events that impact navigation and commerce, and shape habitats for marine life, especially in coastal areas [1,2]. Coastal areas are under constant pressure due to intense anthropogenic activities such as urbanisation, exploitation of natural resources, and climate change-induced natural hazards (e.g., coastal erosion due to sea level changes) [1]. The littoral zone of this interface is spatially complex and determines biodiversity-related processes as increasing bathymetric values decrease light penetration and cause changes in habitat compositions and the depth zonation of biota [2]. Studies of the coastal zone—including the modelling of tsunami expansion and wave height estimations, sea-level change scenarios, risk assessment,

and coastal habitat mapping—require the availability or the creation of updated bathymetric data of high (10 m) to very high resolution (2 m) [3–6]. Up to today, numerous researchers have mapped coastal bathymetry with a range of different tools and methods of variable spatial and temporal resolution, but with increased cost. Globally, bathymetry has been extracted by the inversion of the spaceborne geoid data from Geosat and the European Remote Sensing satellite ERS-1 [7] at 12-km spatial resolution as well as from a combination of sound navigation and ranging (SONAR) multibeam sounding data from marine agencies and an improved gravity model from CryoSat-2 and Jason-1 at a 500-m resolution [8]. With respect to currently open access data, Landsat missions, especially Landsat 8 Operational Land Imager (OLI) due to the availability of its coastal/aerosol band 1 centred at a 443-nm wavelength featuring high water penetration) open a new window in coastal satellite-derived bathymetry (SDB) due to their spatial (30-m) and temporal (16-day) resolution. With these characteristics, the Landsat program allows for the selection of proper images (cloud-free or atmospheric images, surface and water column conditions) and the testing of hypertemporal approaches for monitoring changes in seabed morphology [9–11]. The more recently launched Copernicus Sentinel-2 twin-satellite mission has created a new era in terrestrial and marine monitoring due to its high spatial resolution of 10 m, availability of a coastal/aerosol band at 443 nm (60-m spatial resolution), quick revisit time of 5 days, and more significantly, its open and free data access policy. Focusing on SDB, studies have employed Sentinel-2 data in shallow inland waters [12] and semi-closed bays [13,14] with promising results, but not at large scales, with notable differences in the water column and seabed composition. The aforementioned optical sensor technology, machine learning algorithms, and cloud computing system infrastructures provide an unprecedented environment for high spatiotemporal large-scale analysis of natural and anthropogenic ecosystems and associated biophysical variables. Among the available cloud systems, Google Earth Engine (GEE) [15] has attracted the attention of environmental scientists due to its unique components. GEE is a cloud-based geospatial computing platform which offers a petabyte-scale archive of freely available optical satellite imagery. Among characteristics, it features the whole archive of Landsat, the first three Sentinel missions, and full Moderate Resolution Imaging Spectroradiometer (MODIS) data and products. Researchers have utilised it for country-scale vegetation metrics [16], continental-scale mapping of croplands [17], and global land surface temperature [18] and albedo [19] estimation.

　　　Here, we have developed an empirical preprocessing workflow within GEE to estimate four satellite-derived bathymetry algorithms using Sentinel-2 images at three different locations in the Eastern Mediterranean. The preprocessing chain of Sentinel-2 data combines a plethora of simple, widely used, and well-established cloud, atmospheric, and sun glint corrections with a seasonal 10-m image composition approach (median composites). The latter approach opts to reduce the effects of variable water surface conditions, water quality, and related optical properties such as sun glint and sky glint, whitecaps, turbidity, and sedimentation etc. Furthermore, we implement in situ data acquired by a low-cost methodology in the training and validation of the SDB which shows, in turn, promising results for a time- and cost-efficient epoch for wide-scale SDB. We perform the training and validation of the four empirical models in different optically shallow environments to reduce the statistical bias according to the first law of geography by Tobler [20]—spatially neighbouring observations tend to be more similar than the ones further apart. Moreover, we employ a pseudo-invariant-feature (PIF) approach to normalise the differences in the reflectance ranges between the pre-processed composites used in the training and validation steps [21]. Finally, we map the model residuals of the SDB maps to unveil possible over- or under-prediction patterns. Our proposed method can be widely adapted in a cloud computing environment for estimating large-scale coastal bathymetry given, naturally, the availability of relevant open access in situ data.

2. Materials and Methods

2.1. Study Sites and In Situ Data

Figure 1 shows our three study sites; the first study site is Samaria National Park in the southern part of West Crete, Greece, in the Eastern Mediterranean. The selected area covers the east part of the National Park. Mixed habitats cover the seabed here, while depths vary from smooth areas to steep ridges and provide a challenging seascape for space-borne coastal bathymetry. Seagrass meadows reach depths of 40 meters [22]. Bathymetric data was collected during the period 2012–2015 by means of a 5-m inflatable boat using a Lowrance High Definition System (HDS)-5 single-beam echosounder with the HST-WSU 83/200 kHz Skimmer Transducer. The Global Positioning System (GPS) was positioned on top of the roll bar, directly above the transducer to record the exact position. Data was recorded with a frequency of 1 Hz. Preprocessing of Lowrance files was performed using DrDepth software. Data was imported in ArcMap 10.5 in comma separated value (CSV) format and converted into a three-dimensional shapefile for further use. The second study site is Apokoronas area (Obros Gyalos) in West Crete, close to Georgioupolis Bay. It is a remote area with a mixed bottom—shallow rocky reefs followed by bright white sand substrate, ending with seagrass meadows which are followed by a mixed pebble/sand substrate. In this location, the first diving park in Crete is under development, acting also as a protected marine area. Bathymetric data was collected following the aforementioned methodology. The third study site is at Nea Moudania (Thermaikos) in the SouthEast part of the greater Thermaikos Gulf, NorthWest Aegean Sea, Greece. Several types of human activity, including agriculture, aquaculture, industry, tourism, fishing, and trade directly affect the coastal system of Thermaikos. The seascape is mainly made by soft substrates followed by dense continuous seagrass meadows down to approximately 16.5 m. All the aforementioned habitats have been verified by snorkelling and diving. Bathymetric data was collected between 10 and 13 July 2016, utilising the Garmin Fishfinder 160C with an 80/200 kHz (dual beam) sonar. The different transducers in use are due to the availability of the systems at the employed boats. Data was corrected for position, adding the distance from the transducer to the GPS in postprocessing. We calculate the mean depth values that fall within each Sentinel-2 10-m pixel prior to the analysis. Both bathymetry and Sentinel-2 are referenced with respect to World Geodetic System (WGS) 84 (G1762). Additionally, as the whole Aegean basin is a principally tideless environment (mean tide amplitude of a few cm), we assume an identical vertical datum for all the images within the implemented median composite (as seen in Section 2.2; 1 August–31 December 2016) and the singlebeam echosounder data.

2.2. Sentinel-2 Data Preprocessing

A plethora of factors affect the state of the atmosphere (e.g., haze, aerosols, and clouds), sea surface (e.g., sun glint, sky glint, and white caps) and water column (e.g., sedimentation, turbidity and variable optical properties) hindering the remote sensing of the optically shallow extent (where part of the water surface remote signal contains a bottom signal). A suitable preprocessing approach which precedes the estimation of bathymetry from remotely sensed images should address and correct most of these impeding factors. Google Earth Engine's open petabyte-scale satellite image archive allows unprecedented, on the fly, multi-image processing in the cloud. This offers the opportunity to address the hindrances which are inherent in the nature of optically shallow water remote sensing. As such, we implement a preprocessing workflow (Figure 2) that features a combination of metadata information, widely used algorithms in the field of coastal aquatic remote sensing, image composition (median composite), image normalisation, and smoothing. We applied the preprocessing workflow on Sentinel-2 (S2) Level-1C (L1C) top of atmosphere (TOA) data which is the standard S2 archive in GEE (ImageCollection ID: COPERNICUS/S2). Seven S2 bands (coastal aerosol: b1, blue: b2, green: b3, red: b4, near infrared (NIR): b8, shortwave infrared (SWIR) 1: b11, quality assurance (QA) 60 band) form this data input which spans the period between 1 August and 31 December 2016, which is close

chronologically to the acquisition of all in situ bathymetry data and is when the water column is better stratified in the study areas [23]. Our preprocessing workflow consists of seven steps:

1. We employ the QA60 bitmask band which contains cloud information to mask out opaque and cirrus clouds and scale S2 L1C TOA data by 10,000 (S2 quantification value).

2. We use a classification and regression tree (CART) classifier [24] on a b3-b8-b11 composite to mask the terrestrial environment. It is noteworthy that although the classifier is trained with selected aquatic and terrestrial points (35 and 32, respectively) around Crete Island only (Figure 1d), it is utilised in all three sites.

3. To atmospherically correct the masked for clouds and land images, we implement a modified dark pixel subtraction (DPS) method after [25] which subtracts the mean radiance of optically deep-water pixels (>40 m) to address path radiance and two standard deviations to address sensor-related noise in all bands.

4. We employ the so-called image composition where a new pseudo-image is created using—in our case—the median values of the already pre-processed images [16]. This approach aims to further reduce image artefacts which have not been corrected by the previous preprocessing steps. In fact, 79 tiles (34 SGE, 34 SGD, 35 SKV and 35 SKU; also called granules—100×100 km^2 ortho images projected in Universal Transverse Mercator UTM/WGS84 [26]) form the Samaria National Park and Apokoronas pseudo-image, while 18 tiles (34 TFK) form the Thermaikos pseudo-image.

5. We apply the sun glint correction algorithm from [27] to the median composite. Following a user-defined set of pixels that represents sun glint of variable intensity (two polygons in the south of tSamaria National Park site in South Crete), the algorithm equals the sun glint-corrected/sun glint-polluted median composite reduced by the product of the slope of the regression of NIR b8 against b1–b4 and the difference between b8 and its minimum value. We should state here that in [28], the preprocessing step included the mean and not the minimum NIR signal over optically deep water. The two last steps of our preprocessing chain are performed in a GIS environment (ArcMap 10.5) as we export the sun glint-corrected median composites from the previous step for all three areas of interest.

6. We implement the pseudo-invariant features (PIF) [21] to radiometrically normalise b2 and b3 bands which are used in the validation of the SDB models (Apokoronas and Thermaikos composites; Figure 1a,b) to the b2 and b3 of the National Samaria Park composite (Figure 1c). This technique was developed to quantitatively transform a subject multispectral image to the reference multispectral image as if they were sensed under the same atmospheric conditions, and in the case of a coastal study, the same water surface and column conditions. The PIF-based composite normalisation is employed here to decrease the spectral differences which caused high RMSEs in our first SDB validation experiments (results are not shown here). Figure 3 displays the location of the selected PIF features (44 in total for each site), with shallow sands as the bright features and *Posidonia oceanica* seagrasses (National Samaria Park and Thermaikos) and brown algae (Apokoronas; mainly *Cystoseira* sp.) as the dark features. Figure S1 shows the linear equations which are utilised in the radiometric normalisations. We select these specific features because they occupy the extremes (high, low) of the observed reflectance range in all three sites following the recommendations that can be found in [29]; the underlying assumption here is that the PIF changes little between the same tiles (=same site) and different composites (=different site).

7. We apply a 3×3 low pass filter to the normalised S2 b2 and b3 bands to further reduce noise before the training and validation of the empirical SDB models.

2.3. Empirical Satellite-Derived Bathymetries (SDB)

Generally, empirical SDB methods require certain bands in the visible wavelength, with blue and green being the most widely used (as independent variables), and a set of known in situ depths

(the dependent variable) as the only inputs in simple or multiple linear regressions which lead to bathymetry estimations in a given area. Here, we implement and compare four different empirical approaches to derive bathymetry from the pre-processed GEE Sentinel-2 composites. To be consistent in our comparison with the other SDB models and the existing SDB literature, we exploit only the blue and green S2 wavelengths (b2: 496.6 and b3: 560 nm for S2A) in the estimations due to their reasonable water penetration. The training of all four models takes place in the National Samaria Park, while the validation was performed in two different areas: the Apokoronas area and the Thermaikos Gulf (Figure 1). Table 1 provides information on the size of the survey area, number of used in situ points, and their depth range. Given the different depth range of the in situ points in the two validation sites (0–25 m in Apokoronas and 0–12 m in Thermaikos), we trained two different sub-models for each one of the four SDB methods to increase the accuracy of the estimated SDB as it is trained and validated using the same depth range. The first and oldest approach is the one proposed by the author of [28] (hereafter Lyzenga85) which assumes a linear relationship between the log-transformed bands and known depth via (multiple) linear regression. The produced coefficients of the regression are then used to train the Lyzenga85 SDB model which forms as:

$$z = h_0 + h_i X_i + h_j X_j \tag{1}$$

where z is the satellite-derived bathymetry, h_0, h_i, and h_j are the coefficients (intercept and slopes), and X_i and X_j are the independent variables (the radiance in the blue and green bands, respectively). For the 0–25-m depth range, the Lyzenga85 model features an R^2 of 0.79 and RMSE of 2.46 m and takes the form:

$$z = -27.85 + 4.95b2 - 14.13b3 \tag{2}$$

while for the 0–12-m depth range, the model exhibits an R^2 of 0.69 and RMSE of 1.39 m:

$$z = -7.76 + 4.76b2 - 8.71b3 \tag{3}$$

The second and third selected approaches follow two modifications of the proposal by [30]—hereafter referred to as modified Stumpf03 and Traganos17 (after its first use in [31]), respectively—concerning the empirical relationship between the ratio of the log-transformed green band to the log-transformed blue band and water depth. The modified Stumpf03 is simply the multiplicative inverse of the original ratio; it employs the blue to green ratio instead of the original green to blue ratio:

$$z = m_1 \frac{\ln{(nb2)}}{\ln{(nb3)}} - m_0 \tag{4}$$

where m_1 and m_0 are the slope and y-intercept, set by the linear regression between the ratio and bathymetry, and n is a fixed constant (1000 in all experiments related to the approach in [31]) to assure the linear response of the logarithmic ratio with depth and that it will remain positive at all points. The m_1 and m_0 values are 44.39 and 33.17 for the 25-m training set (R^2 = 0.59, RMSE = 3.49 m) and 20.37 and 12.16 for the 12-m training set (R^2 = 0.5, RMSE = 1.78 m), respectively. The Traganos17 SDB algorithm is essentially the ratio of log-transformed blue to log-transformed green (x) without the n constant of Equation (4) and has shown more accurate results over low-reflectance bottoms (e.g., seagrasses and algae) than the original algorithm in [30], which was primarily tested in and tuned with high-reflectance bottoms (e.g., sand, coral reefs). The exponential equation:

$$z = 4416.3e^{-6.12x} \tag{5}$$

is implemented to estimate bathymetry in the Apokoronas area (R^2 = 0.67, RMSE = 3.65 m) up to a 25-m depth, while the linear equation with m_1 and m_0 values of 20.37 and 12.16, respectively, derives bathymetry of up to a 12-m depth in the Thermaikos Gulf (R^2 = 0.56, RMSE = 1.68 m). The fourth and final SDB empirical approach is the one developed by the authors of [32] (hereafter Dierssen03), which

takes the log-transformed ratio of the blue to green median composite (*x*) here (green to red band in the original paper) to map bathymetry. The exponential equation:

$$z = 9.46e^{1.52x} \tag{6}$$

is used to estimate the bathymetry in Apokoronas ($R^2 = 0.66$, RMSE = 3.59 m) in the 0–25-m depth range and the linear equation:

$$z = 7.05 \ln\left(\frac{b2}{b3}\right) + 8.31 \tag{7}$$

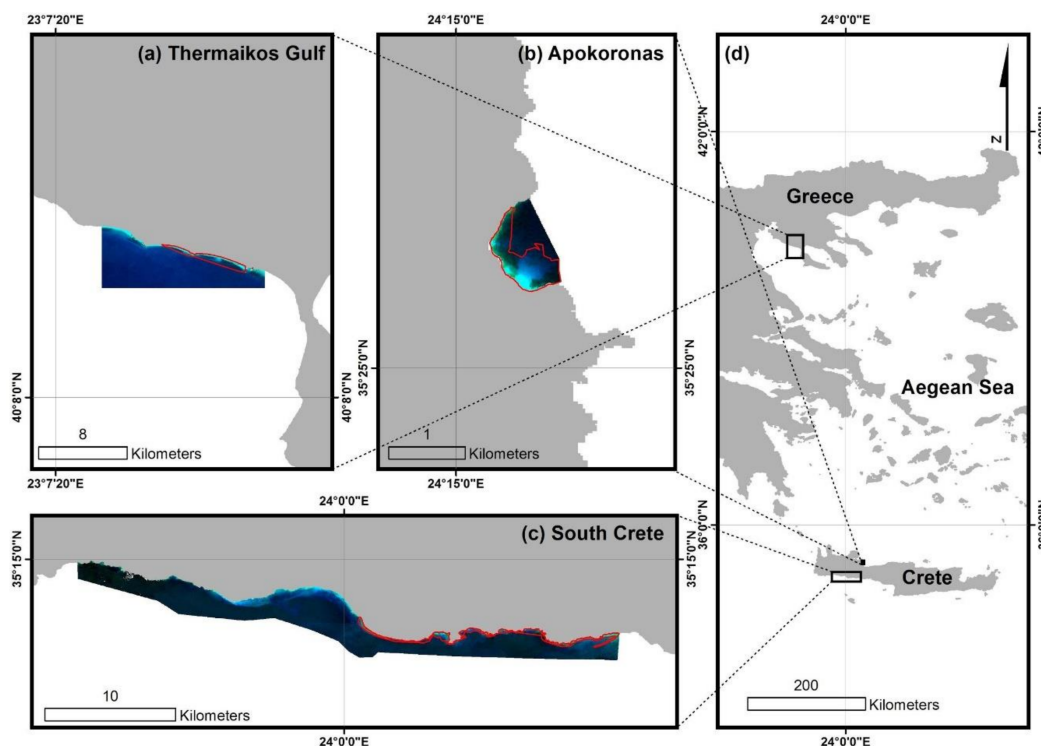derives the bathymetry in Thermaikos in the 0–12 m depth range ($R^2 = 0.53$, RMSE = 1.72 m).

Figure 1. Locations of selected study sites for bathymetry model analysis: (**a**) Thermaikos Gulf; (**b**) Obros Gyalos in the Apokoronas area; (**c**) National Samaria Park, South Crete; and (**d**) the Aegean Sea, Greece. The red polygons indicate the extent of the area that is used for the actual analysis. All depicted images are median Sentinel-2 composites using the preprocessing workflow from Figure 2.

2.4. Spatial Distribution of Model Residuals

As our studied seabed varies from bright shallow sand to dark seagrass meadows and algae-covered bottoms, we expect related errors in the resulting SDB maps. To further distil the spatial information from the SDB maps, we calculate the distribution of model residuals. We estimate the latter as the remainder of the subtraction of the in situ bathymetry data from the most accurate trained and validated SDB maps (Lyzenga85 in all three areas). Following the suggestions by the authors of [33], spatial error maps are derived by Kriging interpolation (ArcMap Spatial Analyst tool) of the remaining points to the whole extent of the training and validation sites to unveil over- and under-prediction patterns of the SDB models. The Kriging interpolation algorithm utilises a spherical semivariogram model and a variable search radius of 12 points to "capture both the deterministic and autocorrelated variation in the residual surface" [33].
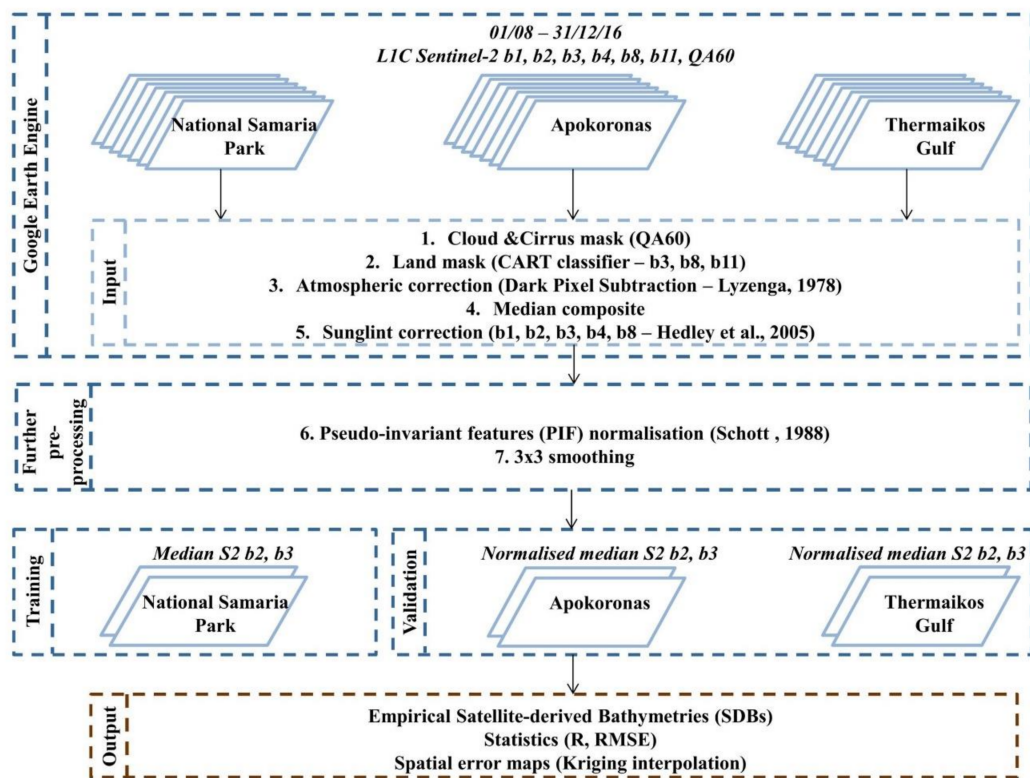
Figure 2. The methodological workflow of the present study. We employ seagrass and algae beds as dark features and shallow sand as bright features; We perform the training of the satellite-derived models in the National Samaria Park sites using two different depth ranges to capture the representative depth range in the validation sites: 0–25 m in Apokoronas and 0–12 m in Thermaikos.
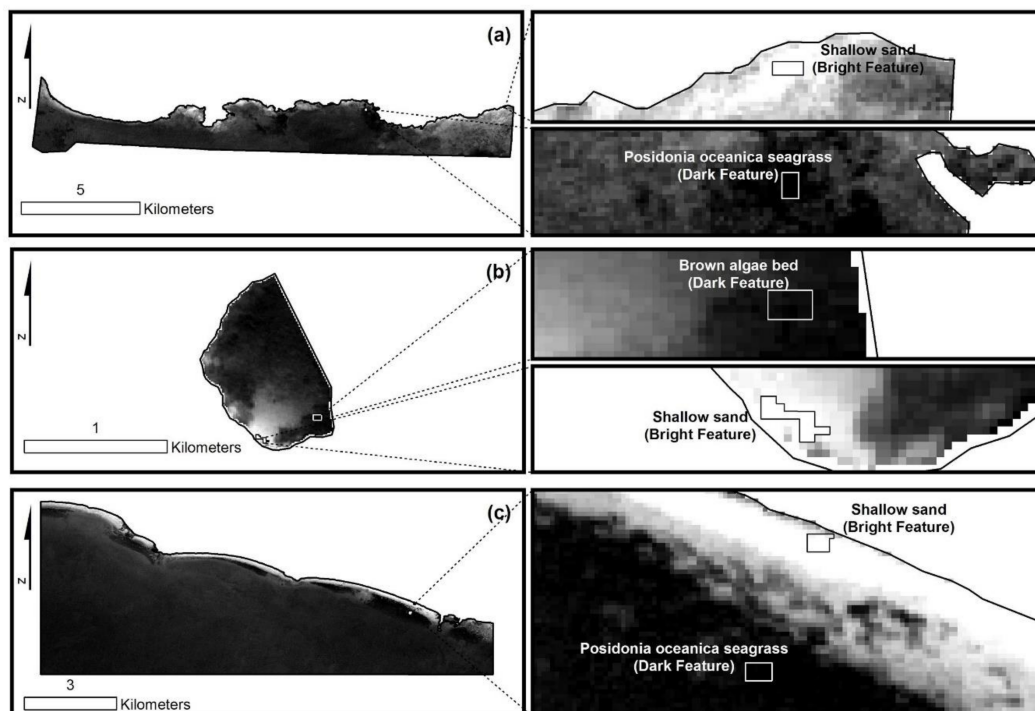

Figure 3. Location of used pseudo-invariant features (zoomed right panels) in the normalisation of the Apokoronas and Thermaikos composites (**b**,**c**) to the National Samaria Park composite (**a**).

Table 1. Survey area and number of related in situ points used for training and validation of the satellite-derived bathymetry models. The Thermaikos Gulf has a lower number of validation points as the initially available dataset is much smaller in comparison to that of Apokoronas.

Survey Site	National Samaria Park (Training)	Apokoronas (Validation)	Thermaikos Gulf (Validation)
Survey area (km^2)	46.3	1.3	20.6
Number of in situ points	4978 (25-m models) 3230 (12-m models)	1557	53
Depth range and intervals of in situ points (m)	0–25: 0–5 (675), 5–10 (1998), 10–15 (1247), 15–20 (659), 20–25 (399) 0–12: 10–12 (556)	0–25: 0–5 (57), 5–10 (301), 10–15 (428), 15–20 (517), 20–25 (254)	0–12 0–5 (25), 5–10 (26), 10–15 (2)

3. Results

3.1. SDB Estimations

Figure 4 shows the pre-processed median S2 composites and their respective satellite-derived bathymetry maps of the training (Figure 4a,b) and validation sites (Figure 4b,c,e,f). Maximum SDB depths are 27 m in National Samaria Park, 23 m in Apokoronas, and 16 m in the Thermaikos Gulf (minimum depth of Thermaikos is 1.7 m, 0 in the two other sites). All statistical results are collectively given in Tables S1 and S2. In terms of validation, the Lyzenga85 model achieves the best accuracies, explaining 90% of the variation inside the validation dataset at Apokoronas (Figure 5—1557 points; RMSE = 1.67 m) and 86% of the variation inside the validation dataset at Thermaikos (Figure 6—53 points; RMSE = 4.1 m). More specifically, with regard to the Apokoronas area, the Lyzenga85 approach features approximately twelve-fold higher R^2 and five-fold smaller RMSEs than the average R^2 and RMSE values of 0.073 and 8.84 m, respectively, for the modified Stumpf03, Traganos17, and Dierssen03 approaches. On the other hand, with regard to the Thermaikos area, the Lyzenga85 model explains 2.6 times better the variation within the validation dataset than the average 33% of the other three models, but exhibits a 1.49-m greater RMSE than their average value of 2.6 m. The utilisation of the Traganos17 SDB model yields the lowest RMSE of 2.49 m here ($R^2 = 0.52$).

3.2. Methodological Gains Using a PIF Normalisation and 3×3 Smoothing

Figure 5 demonstrates the effectiveness of including pseudo-invariant-feature-based normalisation and a 3×3 low pass filter over the remotely-sensed composite before the validation of the SDB models. All four panels in Figure 5 are the validation plots of the model with the highest accuracy (Lyzenga85) in the Apokoronas area which differ in terms of the incorporated preprocessing methods. The validation on a pre-processed composite utilising only the five first steps of Figure 2 (Figure 5a) results in an R^2 of 0.89 and a RMSE of 3.79 m, which is nearly halved to 1.92 m (same R^2) by normalising the pre-processed composite prior to the validation (Figure 5b). The application of 3×3 smoothing without the normalisation (Figure 5c) produces the highest RMSE of 4.79 m (nearly same R^2 of 0.88), whereas with normalisation (Figure 5d), we observe that R^2 rises marginally by 0.02, and the RMSE drops to 1.67 m in comparison to step 3.
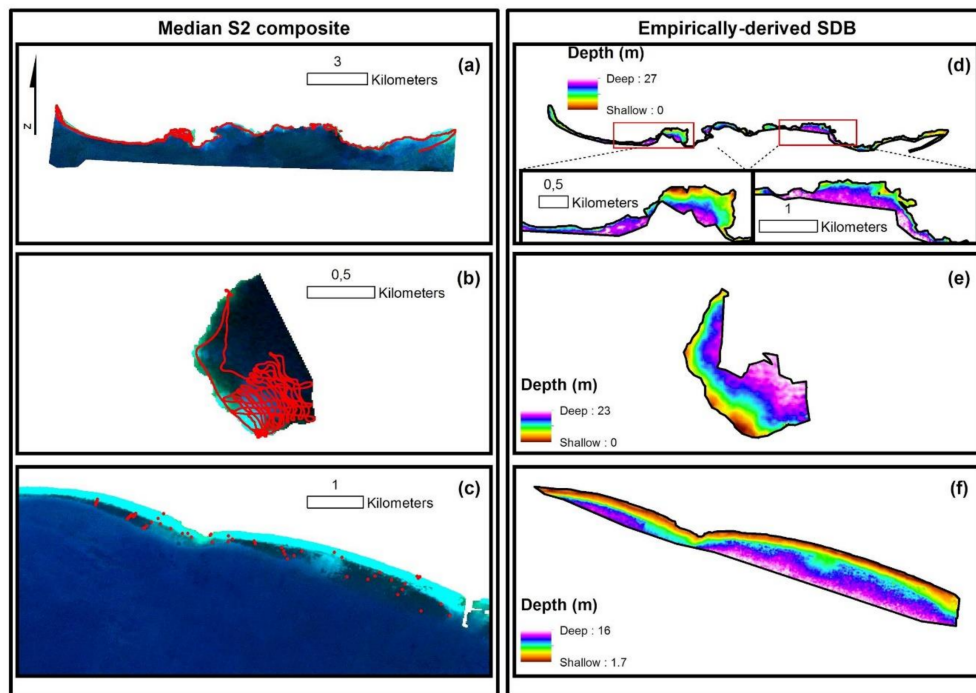
Figure 4. Pre-processed median Sentinel-2 composites using the workflow of Figure 2 on the left panels (**a**–**c**) and related best empirical satellite-derived bathymetry (SDB) estimates on the right (**d**–**f**): The National Samaria Park composite and related SDB estimates in panels (**a**,**d**); Apokoronas composite and related SDB estimates in panels (**b**,**e**); Thermaikos composite and related SDB estimates in panels (**c**,**f**). Red points depict the employed in situ points in the training (**a**) and validation (**b**,**c**) of the SDB models here. Best algorithm (highest R^2, lowest RMSE) in all three cases is Lyzenga85 model applied on 3 × 3 smoothed and normalised median Sentinel-2 composites using the shown pseudo-invariant (PIF) features in the zoomed maps of Figure 3b.

3.3. Spatial Distribution of Model Residuals

Figure 7 depicts the spatial variation of the model residuals of the SDB maps following training by the Lyzenga85 model. In conjunction with the validation plots in Figures 5 and 6, the three figures reveal potential geographical- (horizontal) and depth-related (vertical) patterns of over- or under-prediction (always as a reference to the used in situ data) and the relation of the latter to the presence of specific habitats. There are several distinctive over- and under-prediction SDB patterns. First, the National Samaria Park area (training site) features an under-prediction and over-prediction tendency in its westernmost and easternmost parts, respectively (Figure 7a). There are also model residuals related to under-prediction over shallow sand and rocks of less than ~6 m and more than ~21 m (Figures 3a, 4d and 7a). Second, the Apokoronas area (first validation site) shows variable prediction trends across variable depth zones—the Lyzenga85 model underpredicts bathymetry in approximately the first 6 m over the sand-covered seabed and in the algae-covered seabed deeper than approximately 17 m (Figures 3b, 4e and 7b). The latter is further justified by the validation plot (4) of Figure 5 which displays an under-estimation of depth towards the deeper seabed in Apokoronas. The remainder of the bottom of the same site—which is dominated by algae habitats—depicts an over-prediction of SDB (Figure 7b). Third, the residuals in the Thermaikos Gulf (second validation site) are all related to over-prediction, which ranges between 3 and 4.9 m. While the westernmost and easternmost Thermaikos' seabed, covered with dense *P. oceanica* seagrass and sparse *Cymodocea nodosa* seagrass, exhibit the greatest degree of over-prediction, the central Thermaikos, covered by a smaller *P. oceanica* meadow, lays out a smaller degree of over-prediction with a rising tendency from west to east (away from the centre of the composite) (Figure 7c). Last but not least, we note medium

over-prediction values (off-white colour) over the sandy bottom in the northwestern and southeastern areas. This is greater than for the studied central Gulf.
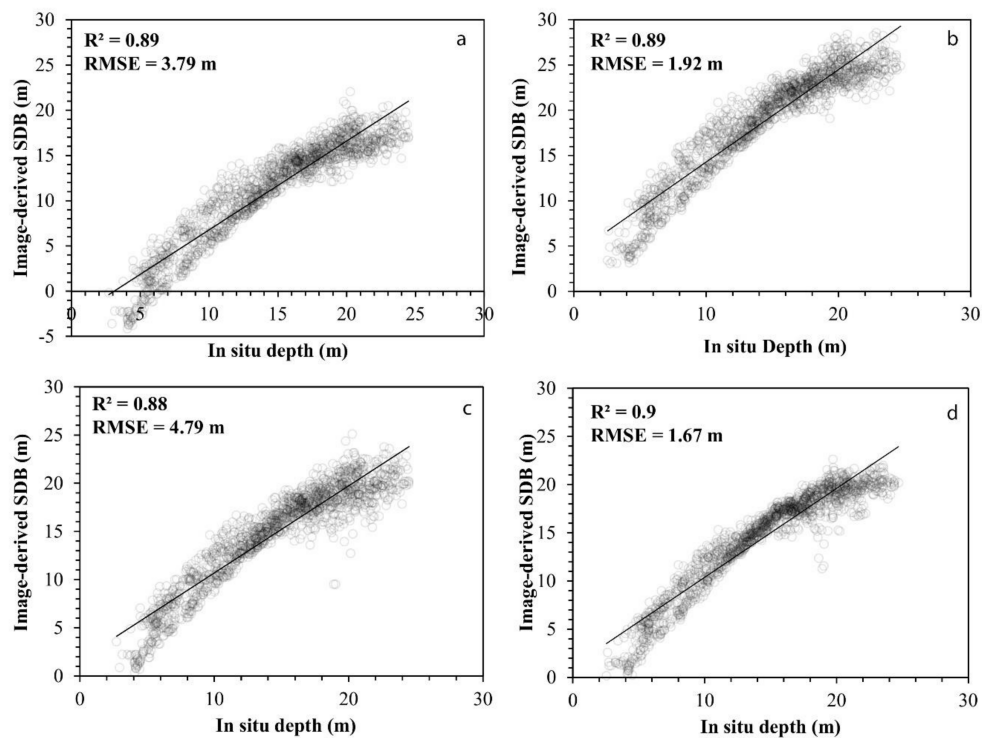

Figure 5. Validation plots of in situ depth points (*x*-axis) against image-derived bathymetries (*y*-axis) implementing the Lyzenga85 model which displays the best accuracy from the median Sentinel-2 composites of Apokoronas site for successive methodological steps including: (**a**) the initial median Sentinel-2 composite; (**b**) a normalised median Sentinel-2 composite using the shown pseudo-invariant (PIF) features in the zoomed maps of Figure 3b; (**c**) a 3 × 3 smoothed median Sentinel-2 composite; (**d**) a 3 × 3 smoothed and normalised median Sentinel-2 composite which shows the best accuracy among the four models of the present study in the Apokoronas site.
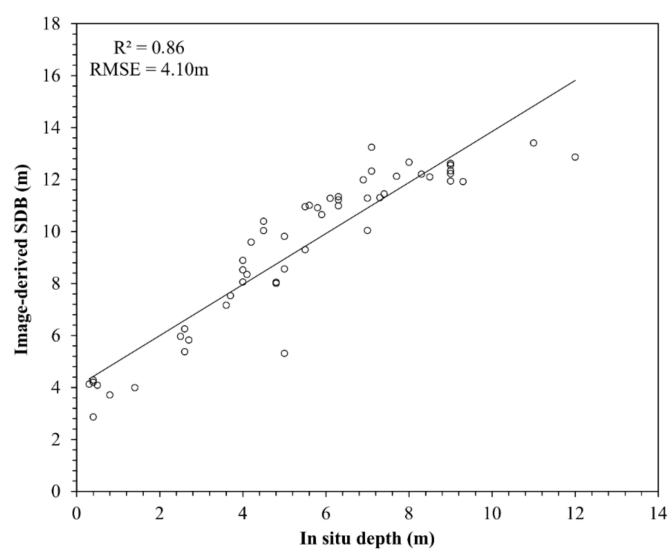

Figure 6. Validation plot of 53 in situ depth points (*x*-axis) against image-derived bathymetries (*y*-axis) employing the Lyzenga85 model on the 3 × 3 smoothed and normalised median Sentinel-2 composite of Thermaikos site.
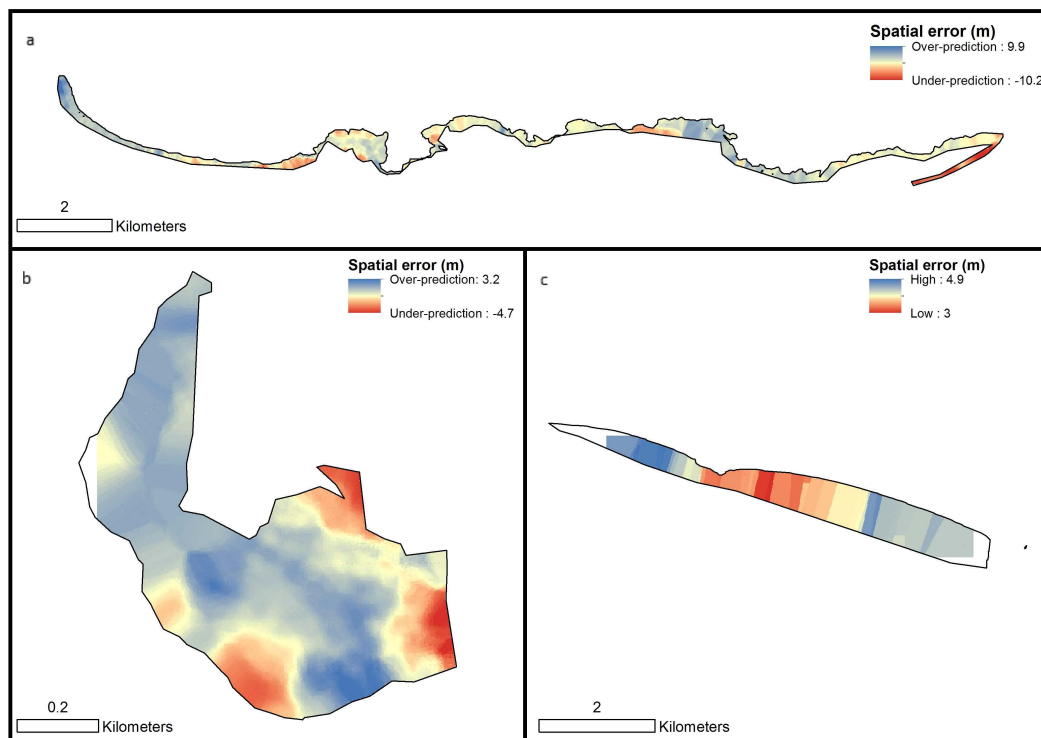
Figure 7. Spatial distribution of model residuals of the SDB maps with the highest accuracy. (**a**) the training site (National Samaria Park, 25-m maximum depth); (**b**,**c**) the two validation sites—Apokoronas in panel b (25-m maximum depth) and Thermaikos in panel c (12-m maximum depth). Note that the upper and lower left ramps indicate over- and under-prediction (as the difference between satellite-derived and in situ bathymetry), while the lower right ramp depicts high to low spatial error (both over-prediction).

3.4. SDB Sensitivity to Variation in Seabed Habitat and Reflectance

To further explore the performance of the SDB models with bottom habitat variability, we examine the two most widely implemented empirical algorithms, Lyzenga85 and Stumpf03, and the blue median reflectance composite (490 nm) along two different transects (0–20-m depth range) in the three study areas (Figure 8). All references to panels in this paragraph are as given for those in Figure 8. All transects run seaward and nearly perpendicularly to the coastline.

Generally, the better performance of Lyzenga85 in comparison to the modified Stumpf03 is exemplified by the smoother variation of the former model with changes in seabed habitats and thus more blue reflectance than in the latter model. Stumpf03 and blue reflectance appear to be more dependent across the majority of transects; at the same time, the Lyzenga85 model exhibits a smaller habitat interdependence (as manifested by variations of blue reflectance), especially over dark-reflectance bottom areas (seagrass and algae) as seen in the upper left (240–500 m), middle right, and lower left panels. Additionally, in comparison to Stumpf03, Lyzenga85 seems to underpredict bathymetry over sandy and rocky habitats, except for the deeper sand (b2 < ~0.015) (upper left and right, middle left, and lower left panels).
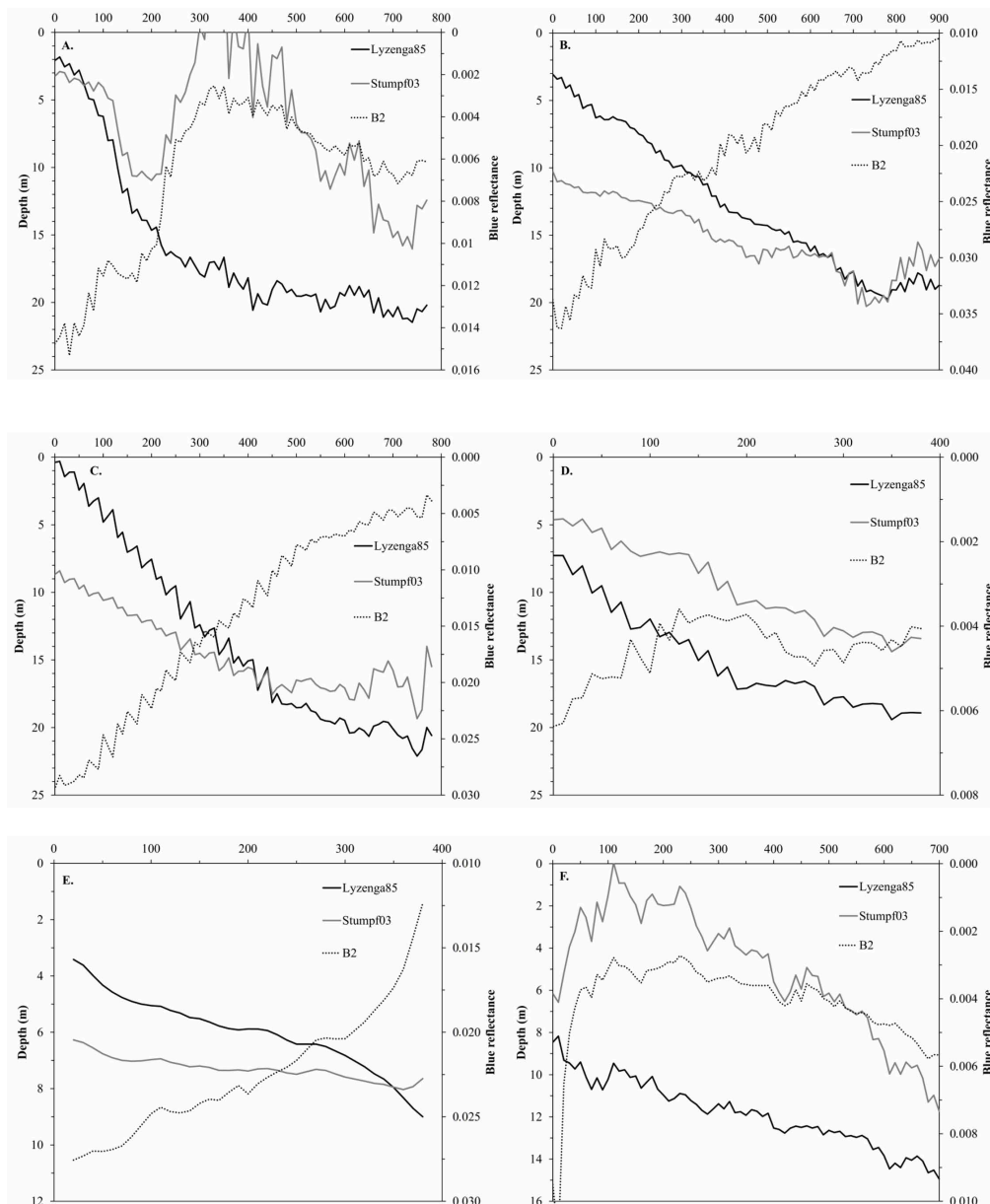
Figure 8. Satellite-derived bathymetry profiles using most accurate Lyzenga85 and modified Stumpf03 models, and a 3 × 3 smoothed and normalised median blue Sentinel-2 reflectance composite (490 nm). (**A**) Samaria National Park: profile over seabed with rocks, sand, and *Posidonia oceanica* seagrass, successively; (**B**) Samaria National Park: profile over sand; (**C**,**D**) the Apokoronas site: profiles over sand and algae-covered beds, respectively; (**E**,**F**) Thermaikos site: profiles over sand and *P. oceanica* seagrass, respectively.

4. Discussion

4.1. Cloud-Based SDB and Model Performance

Cloud-based geospatial analysis platforms, such as the herein utilised Google Earth Engine, provide an unprecedented opportunity for large-scale, on the fly preprocessing, processing, and analysis of vital to the coastal marine environment open data. Here, we developed a preprocessing workflow within GEE and a GIS environment which implements a plethora of widely used and well established algorithms in the remote sensing of optically shallow habitats (seagrasses, corals, algae etc.)

prior to the calculation of four empirical satellite-derived bathymetries [28,30–32] with Sentinel-2 along with their statistics and model residuals.

During the last three decades, a series of empirical, semi-analytical, and analytical methods have been developed for the estimation of optically shallow bathymetry from remote sensing images [34]. Here, we focus on the empirical methodologies which employ linear- or ratio-based statistical relationships between the log-transformed, water-penetrating bands (most frequently at blue and green wavelengths) and acoustic-derived in situ depth data to calculate SDB. Empirical algorithms assume a priori homogeneous water column and bottom composition; this is rarely the case, however, in a typical coastal Aegean benthic site with several seagrasses neighbouring sands and rocks with algal communities within the optical depth limit of the herein used Sentinel-2. Therefore, the non-unique nature of our selected study sites somehow breaches the assumptions of the empirical approaches. Nevertheless, we examine them here due to their historical significance, simple and widespread utilisation, and good accuracy. Among the investigated models in both training and validation in the two depth ranges (0–12 and 0–25 m), the Lyzenga85 model [28] exhibits the highest R^2 and smaller RMSE values on average (0.81 and 2.4 m respectively) followed by the Traganos17 model [31] with an R^2 of 0.45 and RMSE of 4.03 m. The empirical model of Stumpf03 features the poorest overall performance with an R^2 of 0.3 and RMSE of 4.41 m (Table S1 and S2). All models are tuned in the National Samaria Park over primarily sand- and rocky-covered seabed with sparse seagrass patches and validated over the mainly sandy bottom with a few algae in Apokoronas and the dense seagrass beds with few sands and algae in the Thermaikos Gulf (Figure 4). In comparison to unpublished SDB results in the South Cretan training site using the Dierssen03 [33] empirical band ratio of a super-resolved (60 to 10 m) Sentinel-2 coastal aerosol band 1 to green band 3 tuned with the same in situ depth data with the present study (depth range of 0–30 m), the herein Dierssen03 model produces a lower lower R^2 (reduced by 0.19), but also 0.72-m smaller RMSE.

On the other hand, previously published SDB results using Sentinel-2 in the validation site of the Thermaikos [31] with the original Traganos17 algorithm tuned in the same waters at depths between 0 and 20 m explained 1.76 times better the variation, with a 1.19-m smaller RMSE in comparison to the present Traganos17 results. In yet another SDB application in the Thermaikos site [34] with 5-m RapidEye imagery, the use of Dierssen03 empirical ratio exhibited a 0.49 lower R^2 with a decreased RMSE of 0.09 m in comparison to the herein validated Dierrsen03 model. In the previous approaches, training and validation data points originated from the same site and thus were characterised by high autocorrelation according to the first law of geography by Tobler which could have caused statistical bias; here, we attempt to lower this bias by employing two independent in situ data sets in two different sites to validate the calibrated empirical models.

4.2. On the Importance of Image Composition, PIF and the Spatial Distribution of Errors

The ability to create remotely sensed image composites by calculating the median of every pixel in the image across a given time range mitigates in an inter-image fashion intra-image issues related to water surface and water quality conditions, and optical properties; issues like waves, sun glint and sky glint, temporal sedimentation due to land-based rainfall runoffs, or resuspension of seabed sediments due to intensive wave activity for long periods tend to degrade the quality of single images and impede SDB applications. The selected time range affects the composite quality—a short time range could possibly cause data gaps while a long one could amplify the artificiality of the resulting pseudo-image. Here, we selected the time period between 1 August and 31 December 2016, which is chronologically closer to the acquisition of field bathymetry data within the Sentinel-2 lifespan and satisfies the criterion of a better-stratified water column for our study region (Aegean Sea) [23]. Future users of the herein proposed workflow are naturally expected to choose the time range based on the acquisition dates of their in situ data, and the optimum surface and water column conditions of their study area. It is worth mentioning that the temporal difference between data acquisition (2012–2015) and image composition (2016) in our study is not expected to obstruct the SDB estimations because

all three sites are relatively protected from both weather phenomena and coastal processes, hence featuring a stable seabed. While the present work is within a coastal marine environment with almost no influence from tides, when the used methods and the proposed approaches are adopted at areas with tides that affect the results, a correction of the tide using measurements from tide gauges at fixed stations is a mandatory step in the satellite derived bathymetry process.

The radiometric normalization of the median image composites using the pseudo-invariant-feature approach [21] allows the successful development of our approach. The implemented image composites for validation here originate in sites which are approximately 26 (Apokoronas) and 562 km (Thermaikos) (Figure 1) away from the training site (National Samaria Park). This necessitates the utilisation of the PIF normalisation method to correct the two former composites to the reflectance range of the latter composite. The yielded better statistics following utilisation of PIF and 3×3 low pass in combination with the smaller spread of regressed values (Figure 5d) manifest the importance of these two preprocessing steps. The image composition using median values prior to the application of PIF increases the reliability of the subsequent SDB estimations due to the decrease of cross-image composite comparison issues [35]. To the best of our knowledge, this study is the first to employ PIF as a preprocessing step for SDB calculations. Previous uses of PIF normalisation within an optically coastal shallow setting have been confided to its preprocessing implementation for coral bleaching detection [29,36].

The depiction of the spatial distribution of model residuals (Figure 7) is integral here. There are two inherent assumptions in the empirical nature of SDB estimations; first, in situ observations employed in the training and validation of a given SDB model are independent in between them, and second, model residuals feature a normal distribution and random location. The presence of spatial dependence shown by the selection of observations from the same image (and thus in close proximity) adheres to the first law of geography by Tobler but violates the assumed freedom and location of in situ measurements, heightening the standard error and broadly lowering the statistical confidence of the SDB models. On one hand, the origination of both training and validations datasets from the same site is common practice in optically shallow bathymetry derivation studies due to practical reasons (usually the high cost of acquiring such data in the field). On the other hand, the existence of three in situ single beam-derived bathymetry datasets allows us to confront the aforementioned violation, subsequently restricting statistical bias in the results.

The spatial error maps unveil specific over- and under-prediction patterns. Demonstrated more pronouncedly in the National Samaria Park and Apokoronas sites (upper and lower left panel in Figure 7), we identify that mainly algae-covered beds relate to an over-prediction tendency because they comprise a low-reflectance habitat. In the very shallow pixels of Apokoronas, there might be an over-correction by the sun glint algorithm found in [26] due to the interaction of light photons with the seabed in the NIR wavelength which may have decreased reflectance composite values and added to the over-prediction trends. On the contrary, sandy and rocky bottoms reflect more photons, hence producing under-prediction patterns. Generally, the number of photons which reflect on the seabed decreases, and reaches zero past a certain depth limit as averaged by the herein image composition. At this point, the remote sensing signal would contain information arising only from the water column and not the water bottom, therefore being unable to estimate bathymetry. This could have caused the visible under-prediction patterns towards deeper areas independent of the underlying habitat as manifested by the fourth panel in Figure 5 (beyond ~22 m), and the upper and lower left panel in Figure 7 (red colours).

We also show the importance of using the same depth ranges of in situ data for both training and validation of our SDB models, which increase R^2 and decrease RMSE. Implementation of the 0–25 m training in National Samaria Park, validated in the Apokoronas site model in the Thermaikos site and spanning depths of up to 12 m, produces a 0.06 smaller R^2 value and a nearly two-fold smaller RMSE than the final trained Lyzenga85 model within 0–12 m (Figure 6). This has been also mentioned in [34]: "*The optimal performance of bathymetric estimates is like to be achieved when points covering a fully-representative range of depths are present in both datasets*".

4.3. In Situ Data Collection, Crowdsourced Information and an Outlook for SDB

A vital feature of the present study is the use of low-cost tools for the collection of in situ bathymetric data. Usually, such data are collected by expensive state-of-the-art equipment such as airborne lidar data [37] or multibeam echosounder systems [38]. While these tools derive very high-resolution bathymetries, both their spatial coverage and updating of the derived bathymetry are limited and particularly costly at the shallow coastal zone which is practically inaccessible for large boats carrying the acoustic equipment and where the multibeam swath is narrow. Additionally, airborne campaigns require special licenses that are difficult to obtain. Here, we employ commercial off-the-shelf (COTS) solutions with a total cost of less than 1500 euros, which can be utilised at any region of interest.

Another method of in situ data collection is the involvement of crowdsourcing/citizen science data collection methodology [39]. Since 1963, the Cooperative Charting Program between NOAA's Office of Coast Survey and the United States Power Squadron (USPS) has triggered the submission of bathymetric point data to cartographers via the postal service for chart application. Up to today, several initiatives based on the voluntary participation of boat owners with installed hydrographic equipment have been released [35,40], resulting in the provision of bathymetric maps and information on bottom type and vegetation cover in some cases. Most recently, the Nippon Foundation General Bathymetric Chart of the Oceans (GEBCO) Seabed 2030 project was launched at the United Nations Oceans Conference in 2017 with the goal to map the entirety of the world's ocean seabed by 2030. To achieve this unquestionably ambitious goal, the project aims to create a new fleet of research vessels by employing millions of fishing boats, thousands of cargo, cruise, and passenger ships, and private yachts to acquire crowdsourcing multibeam echosounder data [41]. Nonetheless, the extraction of raw data (XYZ) from the existing databases is not yet permitted for the public, but companies and research projects—such as the H2020 BASE-platform (https://base-platform.com/)—have reached an agreement and the first SDB results utilising crowdsourcing data are now available. The accessibility of such raw data is crucial towards a new era for global coastal bathymetry applications using the present proposed methodology. The empirical nature of our methodology, however, raises the computational demands within the GEE due to the estimation of the regressions between the image composition values and water depth—large scales in both space and time could cause the GEE to create a time-out (GEE error message).

In addition to the envisioned new era for large-scale bathymetry, we discuss five near-future endeavours which could directly or indirectly succeed and/or improve the present methodology and study:

1. The implementation of the estimated spatial error parameter as a postprocessing step to increase the statistical accuracy of the empirically derived SDB models following the work in [34].
2. The utilisation of best-available-pixel (BAP) composition, which employs a series of pixel-based scores related to distance to clouds and shadow masks, atmospheric opacity, day of the year etc., instead of image composition across a relevant time series to the user's study region [42].
3. The use of the proposed preprocessing workflow to conduct sea- to basin-wide habitat mapping and monitoring.
4. The incorporation of radiative transfer-based optimisations following the semi-analytical inversion method of [43] or machine learning methods [10,44] for the derivation of bathymetry.
5. The fusion of the Copernicus Sentinel-1 (also available in GEE) and the Sentinel-2 open and free image archive for the development of 10-m topobathymetric digital elevation models (DEMs)—seamless merged elevation products of terrestrial and underwater topography [45] useful for numerous Earth science applications including mapping and modelling of inundation, sediment transport, sea-level rise, and storm surge [46].

5. Conclusions

The present study proposes a complete preprocessing chain in Google Earth Engine—including simple and well-established algorithms in the remote sensing of optically shallow habitats—which

could be easily implemented through the online provided code to estimate satellite-derived bathymetry using Sentinel-2 data and low-cost field data. The user can select a suitable time range of available Sentinel-2 images according to the available in situ depth data and optimum surface and water column conditions of the area of interest. Here, we train four SDB models utilising a pre-processed median composite of 79 S2 tiles in SW Crete (Eastern Mediterranean) and validate them employing 79- and 18-tile composites in NW Crete and the NW Aegean Sea, 26 and 562 km away, respectively. Given the good accuracies of the calibrated model in the two validation sites (R^2 up to 0.9 and RMSE as low as 1.67 m) despite the large horizontal distance, there is emerging potential for upscaling the herein developed SDB model to the whole optically shallow extent of the Aegean and Ionian Seas, hence further exploiting the capability of GEE for big data analysis. To this end, one particular challenge would surely be the existence of relevant field bathymetric data to validate the accuracy of the upscaling effort. The innovation of this work lies mainly in the fact that it is the first that implements the inter-image approach of image composition within GEE to address single-image issues like atmospheric, surface, and water column interferences which obstruct space-borne approaches in the field of aquatic remote sensing. Moreover, in comparison to their exclusion, the inclusion of PIF-based normalisation to match the reflectance range of the training composite to the validation composites along with a 3×3 smoothing to filter remaining noise prior to the SDB calculation notably improve the methodology as manifested by the increased SDB accuracies. On the other hand, regressions which lie in the heart of the empirical models (e.g., sun glint correction, PIF normalisation, SDB estimations) decrease processing time in GEE and could possibly create related time-out errors. This led us to conduct the radiometric normalisation and the SDB calculations outside GEE in this study for the sake of efficiency. In the near future, we aim to integrate these two preprocessing and analysis steps within the GEE platform in addition to adapting the code to also use Landsat 8 images as input. All in all, due to intense anthropogenic activities, coastal ecosystems are on the verge of significant degradation of their ecosystem services; however, Google Earth Engine and Sentinel-2 have created the perfect storm in the last three years for an unprecedented, global-scale, high spatiotemporal mapping of bathymetry and, more broadly, of the immensely vital optically shallow benthos which can in turn empower physical understanding, management and conservation practices.

Supplementary Materials: The following are available online at http://www.mdpi.com/2072-4292/10/6/859/s1.

Author Contributions: D.T. and D.P. conceived the idea, collected the in-situ data, processed the satellite-derived bathymetries, and wrote the paper; B.A. developed the preprocessing code in Google Earth Engine; P.R. and N.C. supervised the development of the present project, from start to finish.

Conflicts of Interest: The authors declare no conflict of interest.

References

1. Paterson, D.M.; Hanley, N.D.; Black, K.; Defew, E.C.; Solan, M. (Eds.) Biodiversity, ecosystems and coastal zone management: Linking science and policy. Theme Section. *Mar. Ecol. Prog. Ser.* **2011**, *434*, 201–301. [CrossRef]
2. Robertson, E. Crowd-Sourced Bathymetry Data via Electronic Charting Systems. ESRI Ocean GIS Forum, 2016. Available online: http://proceedings.esri.com/library/userconf/oceans16/papers/oceans_12.pdf (accessed on 20 April 2018).
3. Li, R.; Liu, J.-K.; Felus, Y. Spatial Modeling and Analysis for Shoreline Change Detection and Coastal Erosion Monitoring. *Mar. Geod.* **2010**, *24*, 1–12. [CrossRef]
4. Omira, R.; Baptista, M.A.; Leone, F.; Matias, L.; Mellas, S.; Zourarah, B.; Miranda, J.M.; Carrilho, F.; Cherel, J.P. Performance of coastal sea-defense infrastructure at El Jadida (Morocco) against tsunami threat: Lessons learned from the Japanese 11 March 2011 tsunami. *Nat. Hazards Earth Syst. Sci.* **2013**, *13*, 1779–1794. [CrossRef]

5. Roelfsema, C.; Kovacs, E.; Ortiz, J.C.; Wolff, N.H.; Callaghan, D.; Wettle, M.; Ronan, M.; Hamylton, S.M.; Mumby, P.J.; Phinn, S. Coral reef habitat mapping: A combination of object-based image analysis and ecological modelling. *Remote Sens. Environ.* **2018**, *208*, 27–41. [CrossRef]

6. Wang, J.; Yi, S.; Li, M.; Wang, L.; Song, C. Effects of sea level rise, land subsidence, bathymetric change and typhoon tracks on storm flooding in the coastal areas of Shanghai. *Sci. Total Environ.* **2018**, *621*, 228–234. [CrossRef] [PubMed]

7. Sandwell, D.T.; Smith, W.H. Marine gravity anomaly from Geosat and ERS 1 satellite altimetry. *J. Geophys. Res. Solid Earth* **1997**, *102*, 10039–10054. [CrossRef]

8. Olson, C.J.; Becker, J.J.; Sandwell, D.T. A new global bathymetry map at 15 arcsecond resolution for resolving seafloor fabric: SRTM15_PLUS. In Proceedings of the AGU Fall Meeting Abstracts, San Francisco, CA, USA, 15–19 December 2014.

9. Pe'eri, S.; Madore, B.; Nyberg, J.; Snyder, L.; Parrish, C.; Smith, S. Identifying bathymetric differences over Alaska's North Slope using a satellite-derived bathymetry multi-temporal approach. *J. Coast. Res.* **2016**, *76*, 56–63. [CrossRef]

10. Misra, A.; Vojinovic, Z.; Ramakrishnan, B.; Luijendijk, A.; Ranasinghe, R. Shallow water bathymetry mapping using Support Vector Machine (SVM) technique and multispectral imagery. *Int. J. Remote Sens.* **2018**. [CrossRef]

11. Pacheco, A.; Horta, J.; Loureiro, C.; Ferreira, Ó. Retrieval of nearshore bathymetry from Landsat 8 images: A tool for coastal monitoring in shallow waters. *Remote Sens. Environ.* **2015**, *159*, 102–116. [CrossRef]

12. Dörnhöfer, K.; Göritz, A.; Gege, P.; Pflug, B.; Oppelt, N. Water Constituents and Water Depth Retrieval from Sentinel-2A—A First Evaluation in an Oligotrophic Lake. *Remote Sens.* **2016**, *8*, 941. [CrossRef]

13. Chybicki, A. Mapping South Baltic Near-Shore Bathymetry Using Sentinel-2 Observations. *Pol. Mar. Res.* **2017**, *24*, 15–25. [CrossRef]

14. Chybicki, A. Three-Dimensional Geographically Weighted Inverse Regression (3GWR) Model for Satellite Derived Bathymetry Using Sentinel-2 Observations. *Mar. Geod.* **2017**, *41*, 1–23. [CrossRef]

15. Gorelick, N.; Hancher, M.; Dixon, M.; Ilyushchenko, S.; Thau, D.; Moore, R. Google Earth Engine: Planetary-scale geospatial analysis for everyone. *Remote Sens. Environ.* **2017**, *202*, 18–27. [CrossRef]

16. Robinson, N.P.; Allred, B.W.; Jones, M.O.; Moreno, A.; Kimball, J.S.; Naugle, D.E.; Erickson, T.A.; Richardson, A.D. A Dynamic Landsat Derived Normalized Difference Vegetation Index (NDVI) Product for the Conterminous United States. *Remote Sens.* **2017**, *9*, 863. [CrossRef]

17. Xiong, J.; Thenkabail, P.S.; Tilton, J.C.; Gumma, M.K.; Teluguntla, P.; Oliphant, A.; Congalton, R.G.; Yadav, K.; Gorelick, N. Nominal 30-m Cropland Extent Map of Continental Africa by Integrating Pixel-Based and Object-Based Algorithms Using Sentinel-2 and Landsat-8 Data on Google Earth Engine. *Remote Sens.* **2017**, *9*, 1065. [CrossRef]

18. Parastatidis, D.; Mitraka, Z.; Chrysoulakis, N.; Abrams, M. Online Global Land Surface Temperature Estimation from Landsat. *Remote Sens.* **2017**, *9*, 1208. [CrossRef]

19. Chrysoulakis, N.; Mitraka, Z.; Gorelick, N. Exploiting satellite observations for global surface albedo trends monitoring. *Theor. Appl. Climatol.* **2018**. accepted.

20. Tobler, W.R. A computer movie simulating urban growth in the detroit region. *Econ. Geogr.* **1970**, *46*, 234–240. [CrossRef]

21. Schott, J.R.; Salvaggio, C.; Vochok, W.J. Radiometric scene normalization using pseudo-invariant features. *Remote Sens. Environ.* **1988**, *26*, 1–16. [CrossRef]

22. Poursanidis, D.; Topouzelis, K.; Chrysoulakis, N. Mapping coastal marine habitats and delineating the deep limits of the Neptune's seagrass meadows using Very High Resolution Earth Observation data. *Int. J. Remote Sens.* **2018**. accepted.

23. Tanhua, T.; Hainbucher, D.; Schroeder, K.; Cardin, V.; Álvarez, M.; Civitarese, G. The Mediterranean Sea system: A review and an introduction to the special issue. *Ocean Sci.* **2013**, *9*, 789–803. [CrossRef]

24. Breiman, L.; Friedman, J.H.; Olshen, R.A.; Stone, C.J. *Classification and Regression Trees*; Chapman & Hall/CRC: Boca Raton, FL, USA, 1984.

25. Armstrong, R.A. Remote sensing of submerged vegetation canopies for biomass estimation. *Int. J. Remote Sens.* **1993**, *14*, 621–627. [CrossRef]

26. European Space Agency (ESA). *SENTINEL-2 User Handbook*; ESA: Paris, France, 2015; p. 64.

27. Hedley, J.D.; Harborne, A.R.; Mumby, P.J. Technical note: Simple and robust removal of sun glint for mapping shallow-water benthos. *Int. J. Remote Sens.* **2005**, *26*, 2107–2112. [CrossRef]

28. Lyzenga, D.R. Shallow-water bathymetry using combined lidar and passive multispectral scanner data. *Int. J. Remote Sens.* **1985**, *6*, 115–125. [CrossRef]

29. Elvidge, C.D.; Dietz, J.B.; Berkelmans, R.; Andréfouët, S.; Skirving, W.; Strong, A.E.; Tuttle, B.T. Satellite observation of Keppel Islands (Great Barrier Reef) 2002 coral bleaching using IKONOS data. *Coral Reefs* **2004**, *23*, 461–462. [CrossRef]

30. Stumpf, R.P.; Holderied, K.; Sinclair, M. Determination of water depth with high-resolution satellite imagery over variable bottom types. *Limnol. Oceanogr.* **2003**, *48*, 547–556. [CrossRef]

31. Traganos, D.; Reinartz, P. Mapping Mediterranean seagrasses with Sentinel-2. *Mar. Pollut. Bull.* **2017**. [CrossRef] [PubMed]

32. Dierssen, H.M.; Zimmerman, R.C.; Leathers, R.A.; Downes, T.V.; Davis, C.O. Ocean color remote sensing of seagrass and bathymetry in the Bahamas Banks by high- resolution airborne imagery. *Limnol. Oceanogr.* **2003**, *48*, 444–455. [CrossRef]

33. Hamylton, S.M.; Hedley, J.D.; Beaman, R.J. Derivation of High-Resolution Bathymetry from Multispectral Satellite Imagery: A Comparison of Empirical and Optimisation Methods through Geographical Error Analysis. *Remote Sens.* **2015**, *7*, 16257–16273. [CrossRef]

34. Traganos, D.; Reinartz, P. Interannual Change Detection of Mediterranean Seagrasses Using RapidEye Image Time Series. *Front. Plant Sci.* **2018**, *9*. [CrossRef] [PubMed]

35. TeamSurv, 2018. Available online: https://www.teamsurv.com/ (accessed on 28 Match 2018).

36. Hedley, J.D.; Roelfsema, C.M.; Chollett, I.; Harborne, A.R.; Heron, S.F.; Weeks, S.; Skirving, W.J.; Strong, A.E.; Eakin, C.M.; Christensen, T.R.L.; et al. Remote Sensing of Coral Reefs for Monitoring and Management: A Review. *Remote Sens.* **2016**, *8*, 118. [CrossRef]

37. Saylam, K.; Hupp, J.R.; Averett, A.R.; Gutelius, W.F.; Gelhar, B.W. Airborne lidar bathymetry: Assessing quality assurance and quality control methods with Leica Chiroptera examples. *Int. J. Remote Sens.* **2018**, *39*, 2518–2542. [CrossRef]

38. Ierodiaconou, D.; Schimel, A.C.G.; Kennedy, D.; Rattray, A. Combining pixel and object based image analysis of ultra-high resolution multibeam bathymetry and backscatter for habitat mapping in shallow marine waters. *Mar. Geophys. Res.* **2018**, *39*, 271. [CrossRef]

39. International Hydrographic Organization. *Guidance on Crowdsourced Bathymetry*; IHO, Monaco Cedex, 2018; p. 55. Available online: https://www.iho.int/iho_pubs/draft_pubs/CSB-Guidance_Document-Ed1.0.0.pdf (accessed on 20 April 2018).

40. BioBase, 2018. Available online: https://www.cibiobase.com/ (accessed on 28 Match 2018).

41. Nippon Foundation-GEBCO, 2018. Available online: https://seabed2030.gebco.net/ (accessed on 2 May 2018).

42. White, J.C.; Wulder, M.A.; Hobart, G.W.; Luther, J.E.; Hermosilla, T.; Griffiths, P.; Coops, N.C.; Hall, R.J.; Hostert, P.; Dyk, A.; et al. Pixel-based image compositing for large-area dense time series applications and science. *Can. J. Remote Sens.* **2014**, *40*, 192–212. [CrossRef]

43. Lee, Z.P.; Carder, K.L.; Mobley, C.D.; Steward, R.G.; Patch, J.S. Hyperspectral remote sensing for shallow waters: 2. Deriving bottom depths and water properties by optimization. *Appl. Opt.* **1999**, *38*, 3831–3843. [CrossRef] [PubMed]

44. Danilo, C.; Melgani, F. Wave period and coastal bathymetry using wave propagation on optical images. *IEEE Trans. Geosci. Remote Sens.* **2016**, *54*. [CrossRef]

45. Collin, A.; Hench, J.L.; Pastol, Y.; Planes, S.; Thiault, L.; Schmitt, R.J.; Holbrook, S.J.; Davies, N.; Troyer, M. High resolution topobathymetry using a Pleiades-1 triplet: Moorea Island in 3D. *Remote Sens. Environ.* **2018**, *208*, 109–119. [CrossRef]

46. Poursanidis, D.; Chrysoulakis, N. Remote Sensing, natural hazards and the contribution of ESA Sentinels missions. *Remote Sens. Appl. Soc. Environ.* **2017**, *6*, 25–38. [CrossRef]